

Interfaces Govern Structure of Angstrom-scale Confined Water

Yongkang Wang,^{1,2} Fujie Tang,³ Xiaoqing Yu,¹ Kuo-Yang Chiang,¹ Chun-Chieh Yu,¹ Tatsuhiko Ohto,⁴ Yunfei Chen,² Yuki Nagata,^{1} Mischa Bonn^{1*}*

¹*Max Planck Institute for Polymer Research, Ackermannweg 10, 55128 Mainz, Germany.*

²*School of Mechanical Engineering, Southeast University, 211189 Nanjing, China.*

³*Department of Physics, Temple University, Philadelphia, Pennsylvania 19122, United States.*

⁴*Division of Frontier Materials Science, Graduate School of Engineering Science, Osaka University, Toyonaka 60-8531, Japan.*

**Correspondence to: nagata@mpip-mainz.mpg.de, bonn@mpip-mainz.mpg.de*

Abstract

Water plays a crucial role in geological, biological, and technological processes. Nanoscale water confinement occurs in many of these settings, including sedimentary rocks, water channel proteins, and applications like desalination and water purification membranes. The structure and properties of water in nanoconfinement can differ significantly from bulk water, exhibiting, for instance, modified hydrogen bonds, dielectric constant, and phase transitions. Despite the importance of strongly nanoconfined water, experimentally elucidating the nanoconfinement effect on water, such as its orientation and hydrogen bond (H-bond) network, has remained challenging. Here, we study two-dimensionally nanoconfined aqueous electrolyte solutions with tunable confinement from nanoscale to angstrom-scale sandwiched between a graphene sheet and CaF₂. We employ heterodyne-detection sum-frequency generation (HD-SFG) spectroscopy, a surface-specific vibrational spectroscopy capable of directly and selectively probing water orientation and H-bond environment at interfaces and under confinement. Remarkably, the vibrational spectra of the nanoscale confined water can be described quantitatively by the sum of the individual water surface signals from the CaF₂/water and water/graphene interfaces until the confinement reduces to angstrom-scale (< ~8 Å). *Ab initio* molecular dynamics simulations confirm our experimental observation. These results manifest that interfacial, rather than nanoconfinement effects, dominate the water structure until angstrom-level confinement.

Main text

Water under nanoconfinement is the subject of increasing focus,^{1–6} because nanoconfinement has the potential to modify water properties from bulk water^{7–9}, and water in nanoconfinement provides a unique platform for chemical reactions.^{10–12} For example, water in nanoconfinement exhibits anomalously low dielectric constant,⁸ engages in weakened/strengthened hydrogen bonding,^{13,14} and undergoes structural phase transition.^{4,5,15} Water, ions under nanoconfinement show extraordinary transport properties.^{16,17} Water molecules are more reactive in nanoconfinement than that in bulk in contact with a surface and spawn the realm of “chemistry in confinement.”^{10–12,18} These anomalous behaviors of water in nanoconfinement are usually ascribed to the “nanoconfinement effect”. In many studies of properties of confined water, deviations from bulk theory expectations already appear at modest (~10 nm) confinement.⁸ An urgent and important question is whether these effects are due to nanoconfinement effects on the water itself, or rather due to “interfacial effects”,¹⁹ which states that the properties of water under nanoconfinement are altered by water in contact with two interfaces. Indeed, the structure of interfacial water also differs from bulk water, with a truncated hydrogen bond (H-bond) network and ordered structure due to the interaction with the surface.^{20,21} A fundamental question regarding the “nanoconfinement effect” is at what level of confinement, the “nanoconfinement effect” on water starts to appear so that the structure of water under nanoconfinement deviates from the cooperative “interfacial effect”.

To address the question and differentiate between “interfacial” and “nanoconfinement effects” on water, molecular-level insights into nanoconfined water and interfacial water, such as their orientation and H-bond structure, are necessary. To this end, heterodyne-detection sum-frequency generation (HD-SFG) spectroscopy is uniquely suited, owing to three advantages: molecular specificity (in particular, sensitivity to hydrogen bonding strength and molecular orientation); interface and confinement specificity; and additivity of the molecular water response. In an SFG

experiment, infrared and visible laser fields are mixed to generate the sum frequency of those two fields. The signal is enhanced when the infrared (IR) frequency is resonant with the molecular vibration, providing molecular structure specificity.²² Furthermore, HD-SFG spectroscopy provides complex-valued $\chi^{(2)}$ spectra and the sign of the imaginary part of the $\chi^{(2)}$ spectrum ($\text{Im}\chi^{(2)}$) reflects the absolute orientation of water molecules (*up-/down*-orientation).²³ SFG signals are non-zero only when centrosymmetry is broken such as at water interface^{20,24,25} or nanoconfinement-induced alignment of water.²⁶ Signals from the bulk water are naturally excluded due to the SFG selection rule.²⁷ As such, it can selectively probe the water experiencing “the nanoconfinement effect” and the “interfacial effect”. Furthermore, an HD-SFG signal ($\text{Im}\chi^{(2)}$) is additive and thus allows us to quantitatively disentangle the contributions from the two interfaces and the nanoconfinement in the nanoconfined system. With these advantages, one can directly compare the structure of the nanoconfined water with the structure of the interfacial water as an edge of the bulk water, opening a path to distinguish the difference between the “interfacial effect” and the “nanoconfinement effect” on water.

Nevertheless, applying HD-SFG spectroscopy to the realm of nanoconfined liquids has been challenging owing to 1) the length mismatch between nanofluidic devices and typical laser spots: for extreme (sub-nanometer) confinement, devices are dimensioned below a few hundred of nanometers^{8,16,28} while the SFG probes a spot of $\sim 100 \mu\text{m}$; and 2) the challenge of the IR beam to reach the confined region. We overcome these two challenges by fabricating a centimeter-sized (sub-)nanoconfined water system with tunable confinement from nanoscale to angstrom-scale sandwiched between a calcium fluoride (CaF_2) substrate and a graphene sheet. Both the CaF_2 substrate and the graphene sheet allow the IR beam to reach the confined surface. By applying HD-SFG spectroscopy to the nanoconfined water system with tunable confinement and comparing the nanoconfined water response to the response of water at the CaF_2 /bulk water interface and graphene/bulk water interface, we identify the transition, at sub-nanometer confinement, from water dominated by “interfacial effects”

to that dominated by “nanoconfinement effects”.

A commercially available CVD-grown graphene monolayer on a copper foil was exposed to ammonium persulfate aqueous solution to remove the copper sheet and the obtained graphene sheet was exposed to a 10 mM LiCl solution and was then transferred to the CaF₂ substrate using the wet transfer technique.^{2,6} Using the strong interaction of hydrophilic CaF₂ substrate with water, the CaF₂ substrate is wet, enabling the nanoconfined water sandwiched by the graphene sheet and the CaF₂ substrate (for details, see Methods). The water trapped between the CaF₂ substrate and graphene contains Li⁺ and Cl⁻ ions, in the ~molar range, following evaporation of bulk water (see Supplementary Discussion S1). To characterize the thickness of the nanoconfined water, we carried out atomic force microscopy (AFM) measurements. An AFM image probing the edge of the graphene sheet is presented in Fig. 1a, while a typical height profile indicated by the white line in the AFM image is shown in Fig. 1b. The edge of the graphene sheet is folded over, producing two peaks of ~10 nm height. The data manifests that the region on the left side of the folds is the bare CaF₂ surface and the region on the right side is covered by a graphene sheet (Fig. 1c, for more details, see Supplementary Discussion S2). The height difference between the regions where a graphene sheet covers and does not is 1.14±0.3 nm, appreciably larger than the graphene thickness of ~0.34 nm,² indicating that the graphene sheet and CaF₂ substrate sandwich water and the thickness of the confined water is around 8 Å. *Ab initio* molecular dynamics (AIMD) simulations suggest that the confined water comprises 3 water layers (see Supplementary Discussion S3). In the SFG experiments, a spot of ~100 μm diameter was probed, and care was taken via the double check with AFM to ensure that the probed region contained predominantly the ~1 nm confined water (see Supplementary Discussion S2). Further, to check the quality of graphene, we measured the Raman spectrum of the graphene layer (Extended Data Fig. 1). The absence of the defect-related Raman D-band (~1350 cm⁻¹) indicates that the graphene remains intact and of high quality.²⁹ And the 2D-band and G-band intensity ratio of 3 confirms that the graphene is a monolayer (For more details, see Supplementary Discussion S4).

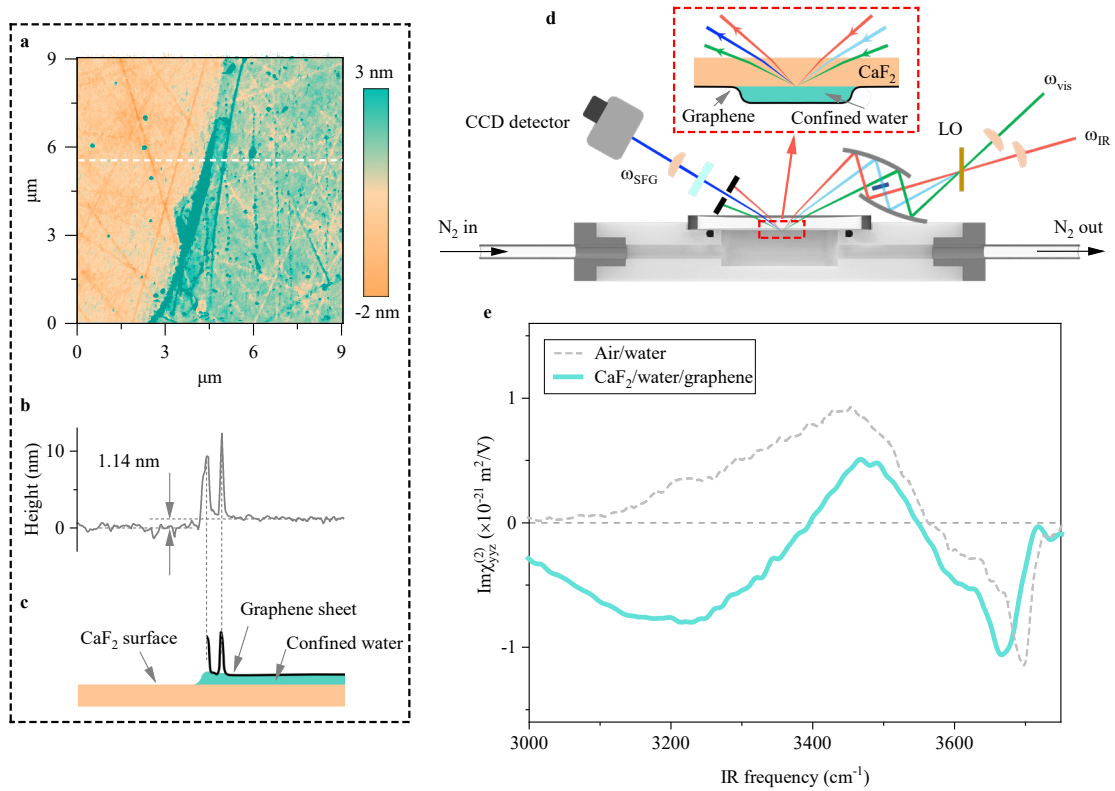


Fig. 1 | HD-SFG detection of sub-nanometer-confined water. **a.** AFM image of the graphene monolayer deposited on the CaF₂ substrate. Measurements were conducted at ambient conditions with a Relative Humidity (RH) of ~25 %. **b.** The height profile along the white dashed line in **b**, crossing the graphene wrinkles. **c.** A schematic of how graphene locks the water on a CaF₂ substrate. **d.** Experimental setup for the HD-SFG measurements. The measurements were conducted at the *ssp* polarization combination, where *ssp* denotes *s*-polarized SFG, *s*-polarized visible, and *p*-polarized IR beams. The sample cell is purged with N₂ at a flow rate of ~0.1 mL/s during the HD-SFG measurement. **e.** The Imχ_{yyz}⁽²⁾ spectrum of (blue) the nanoconfined water sandwiched between the graphene sheet and the CaF₂ substrate. The Imχ_{yyz}⁽²⁾ spectrum of water at the air/water interface (grey) is also shown and is multiplied by -1 for easier comparison. This spectrum was measured using a 5 M LiCl aqueous solution. The dashed line serves as the zero line.

Subsequently, we carried out HD-SFG measurement on the nanoconfined water sample at the *ssp* polarization combination (see Fig. 1d). The obtained Imχ_{yyz,confined}⁽²⁾ spectrum for ~8 Å confined water after correcting for the Fresnel factors is displayed

in Fig. 1e (see Supplementary Discussion S5 and S6). This spectrum exhibits negative 3670 cm⁻¹, positive 3460 cm⁻¹, and negative 3200 cm⁻¹ peaks. Such spectral features differ significantly from the $\text{Im}\chi_{yyz}^{(2)}$ spectrum measured on the air/water interface (Fig. 1e) and that on the CaF₂/water vapor interface (see Supplementary Discussion S7). Independent measurements on different samples indicate the $\text{Im}\chi_{yyz,\text{confined}}^{(2)}$ spectra are highly reproducible (see Extended Data Fig. 2). In the $\text{Im}\chi_{yyz}^{(2)}$ spectrum of the O-H stretch mode, a positive (negative) peak corresponds to the *up*- (*down*-)oriented O-H group to the CaF₂ substrate (to the graphene sheet).^{20,30-32} Furthermore, the low (high) frequency of the O-H stretch peak indicates a stronger (weaker) hydrogen-bonded (H-bonded) O-H group.³³ From its high frequency and its negative sign, one can conclude that the 3670 cm⁻¹ peak indicates the presence of a very weakly interacted O-H group pointing *down* to the graphene sheet.^{20,30} In contrast, the positive 3460 cm⁻¹ and negative 3200 cm⁻¹ peaks indicate that different H-bonded O-H groups vary their orientations inside the nanoconfined water layer.

The interpretation of the SFG spectrum of the nanoconfined water is complicated because two interfaces are probed simultaneously.²⁶ To understand the origin of these SFG features, we further measured the HD-SFG spectra at the CaF₂/bulk aqueous LiCl solution interface, ($\text{Im}\chi_{yyz,\text{CaF}_2/\text{water}}^{(2)}$) and at the suspended graphene/bulk aqueous LiCl solution interface, ($\text{Im}\chi_{yyz,\text{graphene}/\text{water}}^{(2)}$). For brevity, we will refer to the LiCl solution as ‘water’, in the following. Fig. 2a illustrates the $\text{Im}\chi_{yyz,\text{CaF}_2/\text{water}}^{(2)}$ spectrum, while Fig. 2b depicts $\text{Im}\chi_{yyz,\text{water}/\text{graphene}}^{(2)} (= \text{Im}(-\chi_{yyz,\text{graphene}/\text{water}}^{(2)}))$ spectrum showcasing the water/graphene interface for comparison with the ~8 Å confined water signal. This water/graphene interface shows a negative 3670 cm⁻¹ peak, illustrating that the 3670 cm⁻¹ peak for the nanoconfined sample arises from the water-graphene interaction. In fact, molecular dynamics simulation predicted such a peak as the O-H stretch chromophore interacting with the π -orbital of the graphene sheet.²⁰ In contrast,

the bandwidth of the positive 3460 cm^{-1} peak is much narrower for the nanoconfined sample than for the water/graphene interface and the negative 3200 cm^{-1} peak observed for the nanoconfined water sample does not appear at the water/graphene interface. Such a discrepancy in the spectral features can be attributed to the CaF_2 -water interaction. The reduction of the 3460 cm^{-1} peak and the appearance of the 3200 cm^{-1} peak of the $\sim 8\text{ \AA}$ confined water signal could be justified by the broad negative peak ranging from 3000 to 3550 cm^{-1} (Fig. 2a) contributed by water at the CaF_2 /water interface. This broad and negative H-bonded O-H peak arises from the water organization at the positively charged CaF_2 surface at neutral pH (~ 6).³²

Remarkably, the $\sim 8\text{ \AA}$ confined water signal ($\chi_{yyz,\text{confined}}^{(2)}$) can be quantitatively accounted for by the combined CaF_2 /water ($\chi_{yyz,\text{CaF}_2/\text{water}}^{(2)}$) and the water/graphene ($\chi_{yyz,\text{water/graphene}}^{(2)}$) interface signals, i.e.:

$$\chi_{yyz,\text{confined}}^{(2)} = \chi_{yyz,\text{CaF}_2/\text{water}}^{(2)} + \chi_{yyz,\text{water/graphene}}^{(2)} \quad (1)$$

The comparison between the $\sim 8\text{ \AA}$ confined water SFG signal and the sum of the CaF_2 /water and water/graphene signals is shown in Fig. 2c. With no adjustable parameters, the two spectra overlap within the experimental error, manifesting that eq. (1) holds. Such consistency suggests that the $\sim 8\text{ \AA}$ confinement induces no special water structure (H-bond structure or orientational distribution), and the nanoconfined water structure is governed by the interfacial water structure at the two interfaces.

$\chi_{yyz,\text{water/graphene}}^{(2)}$ is insensitive to the LiCl concentration, but $\chi_{yyz,\text{CaF}_2/\text{water}}^{(2)}$ varies with LiCl concentrations (see Supplementary Discussion S1). As a result, the concentration of LiCl solution nanoconfined between the CaF_2 substrate and graphene may affect the validity of eq. (1). Our analysis indicates the $\sim 8\text{ \AA}$ confined LiCl solution in the \sim few molar ranges and we stress within the range of conceivable LiCl (2-8 M) concentrations, eq. (1) holds (see Extended Data Fig. 3). We also note that eq. (1) holds

for different samples prepared using different salts (see Extended Data Fig. 4).

The analysis of the $\text{Im}\chi_{yyz}^{(2)}$ spectra at different sample geometries requires different Fresnel factor corrections and reflectivity corrections^{34,35} (see Supplementary Discussion S5 and S6). Such corrections and underlying assumptions of the interfacial dielectric constant^{36,37} affect the inferred SFG response. To independently corroborate the validity of eq. (1), we simulated the $\text{Im}\chi_{yyz}^{(2)}$ spectra of water for the $\sim 8 \text{ \AA}$ confined water samples, CaF_2 /bulk water sample, and bulk water/graphene sample. Snapshots of the AIMD simulations are shown in Fig. 2d and the data are displayed in Fig. 2e-g respectively.

The simulated spectral lineshapes for the CaF_2 /bulk-water interface, the bulk water/graphene interface, and the $\sim 8 \text{ \AA}$ confined water system closely resemble the experimental data. Furthermore, the simulation clearly demonstrates that eq. (1) holds, i.e., the $\sim 8 \text{ \AA}$ confined water SFG signal is governed by the sum of the SFG spectra at the two interfaces. This corroborates the conclusion from experiments that even with its thickness of $\sim 8 \text{ \AA}$, the structure of the confined water is governed by the interfacial water and the impact of the nanoconfinement does not affect the structure of the nanoconfined water.

The simulations provide further evidence for the negligible impact of the nanoconfinement on the water structure when varying the thickness of the nanoconfined water. As shown in Extended Data Fig. 5, doubling the thickness of the nanoconfined water layer from $\sim 8 \text{ \AA}$ to more than 16 \AA , the changes to the signal are minimal²⁶ manifesting that the impact of the $\sim 8 \text{ \AA}$ confinement on the structure of water is negligible. Our data clearly indicates that the structure of $\sim 8 \text{ \AA}$ confined water is primarily determined by the presence of interfaces, regardless of the presence of the $\sim 8 \text{ \AA}$ confinement.

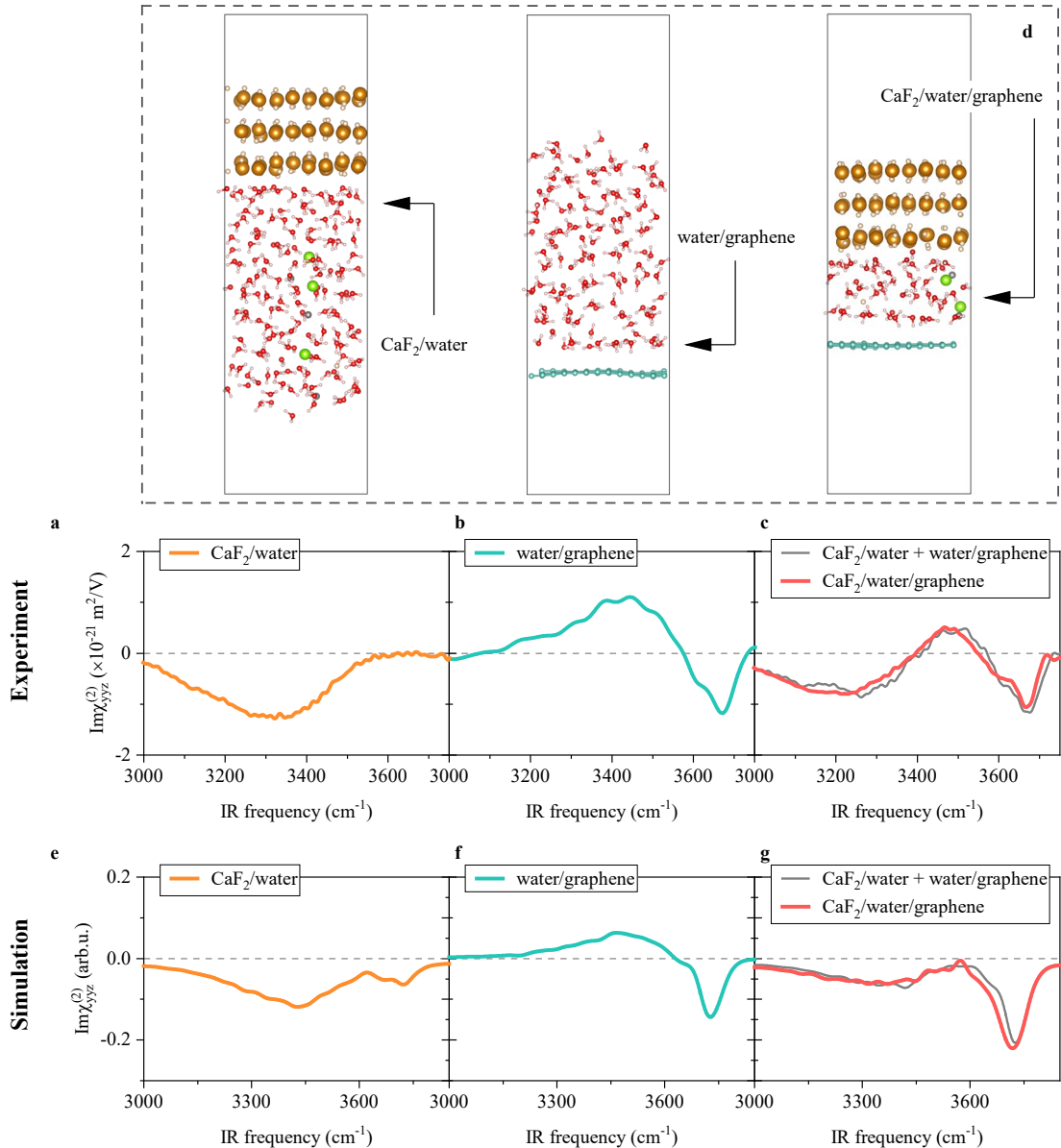


Fig. 2 | Nanoconfined water is governed by interfacial effects. **a, b.** Experimental $\text{Im}\chi_{yyz}^{(2)}$ spectra at the **(a)** $\text{CaF}_2/\text{water}$ interface and the **(b)** $\text{water}/\text{graphene}$ interface. **c.** Experimental $\text{Im}\chi_{yyz}^{(2)}$ spectra of $\sim 8 \text{ \AA}$ confined water. The sum of the $\text{CaF}_2/\text{water}$ and $\text{water}/\text{graphene}$ signals obtained from HD-SFG experiments are also shown for comparison. **d.** Snapshots of the $\text{CaF}_2/\text{water}$ interface, $\text{water}/\text{graphene}$ interface, and $\text{CaF}_2/\text{water}/\text{graphene}$ interfaces obtained from the AIMD simulation. The yellow, light yellow, red, light pink, green, grey, and cyan spheres indicate the Ca, F, O, H, Cl, Li, and C atoms, respectively. We used a 5 M LiCl aqueous solution for the HD-SFG experiments shown in **(a)** and **(b)**. **e, f.** Theoretical $\text{Im}\chi_{yyz}^{(2)}$ spectra of **(e)** the $\text{CaF}_2/\text{water}$ interface; **(f)** the

water/graphene interface; and (g) water confined between CaF_2 and graphene (red line). The sum of the CaF_2 /water (e) and water/graphene (f) signals is shown for comparison (black line). Dashed lines in a-c and e-g indicate the zero lines.

The question arises at what level of confinement, the “nanoconfinement effect” on the water starts to appear so that the structure of water under nanoconfinement deviates from the cooperative “interfacial effect”. To address this question, we measured the $\text{Im}\chi_{yyz}^{(2)}$ spectra on the nanoconfined water sample while reducing the thickness of the nanoconfined water, achieved by progressively lowering the RH in the sample cell through tuning the N_2 flowing rate (Fig. 1d, for more details, see Supplementary Discussion S7). The data are shown in Fig. 3. Upon decreasing the thickness from ~ 8 Å to ~ 5 Å, measured by AFM (see Supplementary Discussion S7), the $\text{Im}\chi_{yyz,\text{confined}}^{(2)}$ spectrum changes substantially. The negative 3200 cm^{-1} peaks and the positive 3460 cm^{-1} peak decrease dramatically, and the 3670 cm^{-1} peak nearly disappears. Such spectral change is more significant with further decreasing the water thickness down to ~ 3 Å. Clearly, Eq. (1) is no longer valid for nanoconfinement below 8 Å. These substantial spectral changes indicate that the “nanoconfinement effect” starts to appear and gradually dominates. The decrease of the two H-bonded O-H peaks and the disappearance of the 3670 cm^{-1} water-graphene peak imply that the <8 Å confinement forces the confined water to lie flat with O-H groups parallel to the graphene and the CaF_2 substrate, consistent with recent theoretical predictions⁴ (for more evidence and discussion, see Supplementary Discussion S7). The parallel-orientated O-H groups yield zero SFG signals, so that the peak intensities decrease. The overall shift of the spectral intensity to higher frequencies denotes that the hydrogen-bonded network is weakened substantially as a result of the enhanced confinement. The HD-SFG measurements on different thicknesses of nanoconfined water demonstrate that the “nanoconfinement effect” on water appears and dominates when the confinement reaches angstrom-scale ($<\sim 8$ Å).

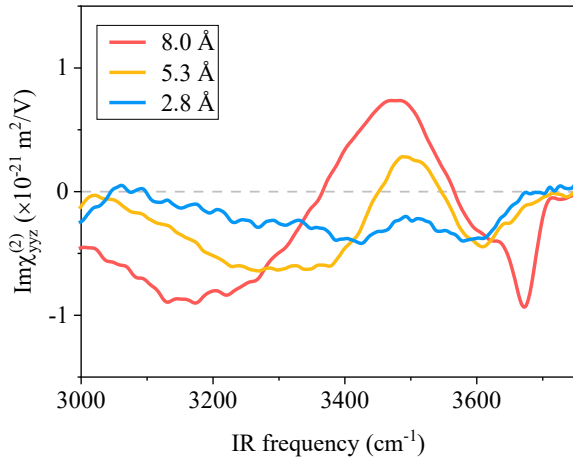


Fig. 3 | Nanoconfinement effect on water. Experimental $\text{Im}\chi_{yyz}^{(2)}$ spectra of the nanoconfined water of different thicknesses. The dashed line indicates the zero lines. The thickness of the nanoconfined water was measured by AFM (For more details, see Supplementary Discussion S7).

Our work addresses the fundamental question related to the “nanoconfinement effect” on water. “Interfacial effect” rather than “nanoconfinement effect” governs the molecular structure of nanoscale confined water until the confinement reduces to angstrom-scale ($< \sim 8 \text{ \AA}$). The revelation of the crucial role of “interfacial effect” on nanoscale confined water ($\geq 8 \text{ \AA}$) could serve to connect the realms of “interfacial chemistry” and “chemistry in confinement”, and offer insight into explaining anomalous phenomena observed in nanoscale confinement, such as the anomalous low dielectric constant of nanoconfined water⁸ and the anomalous ionic transport in nanochannels.¹⁷ Moreover, our findings indicate that for engineering and improving technologies requiring nanoscale confinement, focusing on engineering interfacial properties of the confining materials may suffice when confinement does not occur below $\sim 1 \text{ nm}$. Furthermore, the revelation of the “nanoconfinement effect” on water not occurring until angstrom-scale confinement ($< 8 \text{ \AA}$) illustrates the necessity to create angstrom-scale confinement to induce ‘true’ confinement-induced phenomena. Finally, our work demonstrates that HD-SFG spectroscopy is powerful and highly sensitive to investigate the H-bond network structure and orientation of confined water even for confinement down to angstrom-scale. The findings and experimental capability

established here raise the exciting prospect of future work regarding the probe of molecular details of water and ionic transport in extreme confinement.

Methods

Sample preparation. The samples were prepared by using the wet transfer technique to enclose water between a graphene monolayer and a CaF_2 substrate. We used CVD-grown large-area monolayer graphene grown on copper foil (Grolltex Inc). During the sample preparation, the copper foil was spin-coated with cellulose acetate butyrate (CAB, 30 mg/ml dissolved in ethyl acetate) at 1,000 rpm for 10 seconds, followed by 4,000 rpm for 60 seconds, and then baked at 180 °C for 3 minutes. After cooling down to room temperature, the copper foil/CAB was placed into $\text{HCl}/\text{H}_2\text{O}_2/\text{H}_2\text{O}$ mixture solution (volume ratio, 1:1:10) for 60 seconds to remove the graphene layer grown on the backside of the copper foil. After being rinsed with deionized water, the copper foil on the film was then etched away in 0.1 M ammonium persulfate aqueous solution. Subsequently, the obtained CAB-graphene films were rinsed in deionized water several times to remove residual chemical species, and then were transferred to 10 mM LiCl aqueous solution. Then, the graphene floating on the liquid surface of the LiCl solution was transferred onto the pre-cleaned CaF_2 substrate (see Supplementary Methods). A thin film of LiCl solution was trapped between the graphene and the substrate due to the hydrophilic nature of the CaF_2 substrate. The prepared samples were dried for more than 12 hours at room temperature to remove the excess water. Finally, the CAB layer was removed by immersing the sample in acetone. We note that the $\text{Im}\chi_{yyz,\text{confined}}^{(2)}$ spectra measured on different samples are highly reproducible (For details, see Supplementary S7). We used 10 mM NaCl solution to prepare the nanoconfined water sample, and all reported results were similar (For details, see Supplementary S8). We focus on LiCl because lithium-ion is of interest for its wide application in batteries.

HD-SFG measurement. HD-SFG measurements were performed on a non-collinear beam geometry with a Ti:Sapphire regenerative amplifier laser system. A detailed

description can be found in ref.^{21,32}. HD-SFG spectra were measured in a dried air atmosphere to avoid spectral distortion due to water vapor. The sample cell is purged with N₂ at a flow rate of ~0.1 mL/s during the measurement to remove water vapor in the cell. The flow rate was tuned to change the thickness of the nanoconfined water. To avoid height change of the sample surface during measurements, we used a height displacement sensor (CL-3000, Keyence). Each spectrum was acquired with an exposure time of 2 minutes and measured more than three times on average. The IR, visible, and LO beams are directed at the sample at incidence angles of 33°, 39°, and 37.6°, respectively. The measurements were performed at the *ssp* polarization combination, where *ssp* denotes *s*-polarized SFG, *s*-polarized visible, and *p*-polarized IR beams. More details about the sample preparation, sample cell, HD-SFG measurement, and Raman measurement can be found in the Supplementary Methods in the Supplementary Materials.

Data availability

The data that support the findings shown in the figures are available from the corresponding author upon reasonable request.

Notes

The authors declare no competing financial interest.

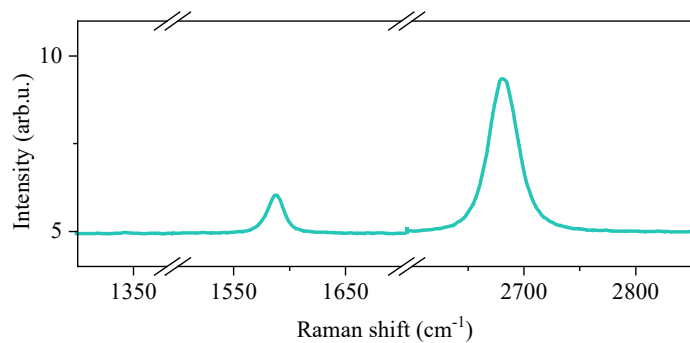
Author contributions

Y.K.W., Y.N., and M.B. designed the study. Y.K.W. prepared the samples and performed the experimental measurements and data analysis. X.Q.Y. independently conducted the HD-SFG measurements at the suspended graphene/bulk aqueous LiCl solution interface. F.T. and T.O. conducted the AIMD simulations. K.Y.C. and C.C.Y. independently conducted the HD-SFG measurements at the CaF₂/bulk aqueous LiCl

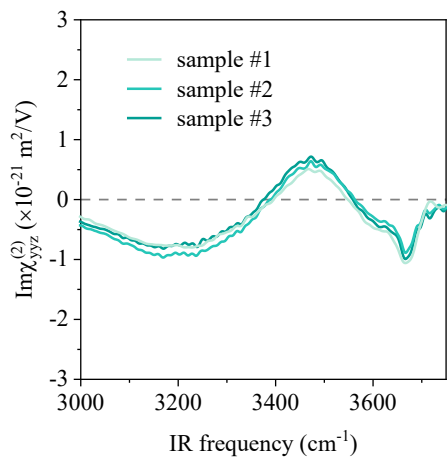
solution interface and on the nanoconfined water sample. Y.K.W., Y.N., and M.B. wrote the manuscript. All authors contributed to interpreting the results and refining the manuscript.

Acknowledgments

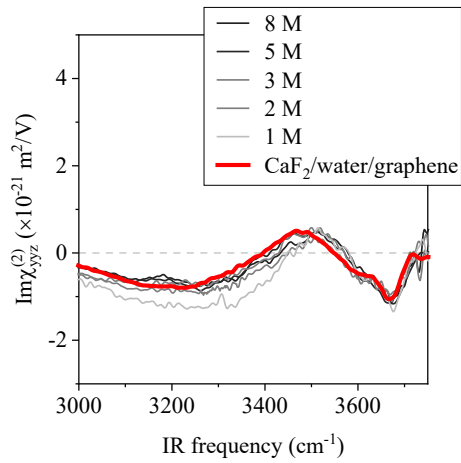
We are grateful for the financial support from the MaxWater Initiative of the Max Planck Society. Funded by the European Union (ERC, n-AQUA, 101071937). Views and opinions expressed are however those of the author(s) only and do not necessarily reflect those of the European Union or the European Research Council Executive Agency. Neither the European Union nor the granting authority can be held responsible for them. We thank Johannes Hunger, Nikita Kavokine, and Maksim Grechko for providing insightful comments and suggestions on this work. We also thank Florian Gericke, Marc-Jan van Zadel, and the technical workshop at the Max Planck Institute for Polymer Research for excellent technical support.



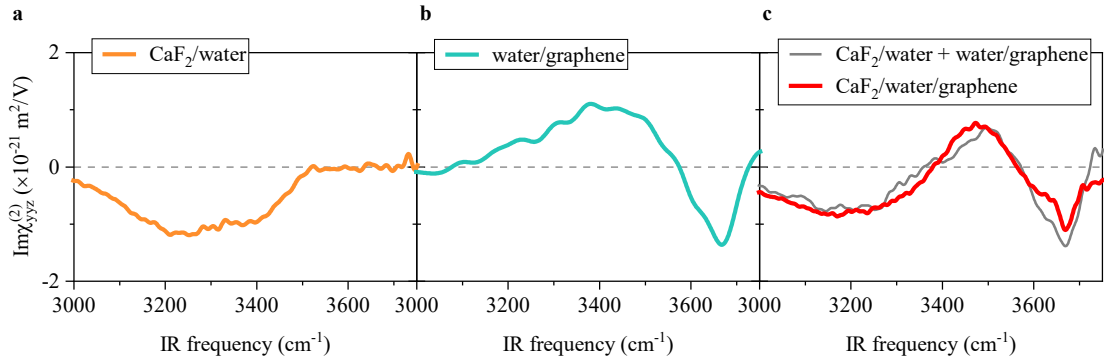
Extended Data Fig. 1 | Raman spectrum of the graphene layer at a randomly selected region.



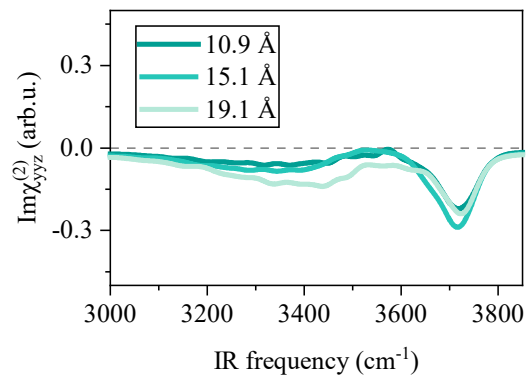
Extended Data Fig. 2 | $\text{Im}\chi_{yyz}^{(2)}$ spectra measured on different samples. The dashed line serves as the zero line.



Extended Data Fig. 3 | The sum of the $\text{CaF}_2/\text{water}$ and $\text{water}/\text{graphene}$ signals obtained from HD-SFG experiments at different LiCl concentrations. Experimental confined water $\text{Im}\chi_{yyz}^{(2)}$ spectrum is also shown for comparison. The dashed line serves as the zero line.



Extended Data Fig. 4 | Negligible ion-specific effect. **a, b.** Experimental $\text{Im}\chi_{yyz}^{(2)}$ spectra at the **(a)** $\text{CaF}_2/\text{water}$ interface and the **(b)** water/graphene interface. **c.** Experimental confined water $\text{Im}\chi_{yyz}^{(2)}$ spectra. The sum of the $\text{CaF}_2/\text{water}$ and water/graphene signals obtained from HD-SFG experiments are also shown for comparison. We used a 5 M NaCl aqueous solution for the HD-SFG experiments of **a** and **b**. The dashed lines in **(a-c)** serve as the zero line.



Extended Data Fig. 5 | Theoretical $\text{Im}\chi_{yyz}^{(2)}$ spectra of nanoconfined water of different thicknesses. The dashed line indicates the zero line.

Supplementary information for “Interfaces Govern Structure of Angstrom-scale Confined Water”

Supplementary Methods

1. Chemicals

All related chemicals of lithium chloride (LiCl), sodium chloride (NaCl), sodium perchlorate (NaClO₄), heavy water (D₂O), sodium hydroxide (NaOH), hydrochloride (HCl, 37%), concentrated sulfuric acid (H₂SO₄, 98%), 30 wt. % hydrogen peroxide solution (H₂O₂), ammonium persulfate ((NH₄)₂S₂O₈), cellulose acetate butyrate (CAB), ethyl acetate, ethanol, and acetone were purchased from Sigma-Aldrich and were all of analytical grade without further purification. Deionized water was provided by a Milli-Q system (resistivity $\geq 18.2 \text{ M}\Omega\cdot\text{cm}$ and TOC $\leq 4 \text{ ppb}$) and was saturated with argon by bubbling gas through it for 30 minutes before use. CVD-grown graphene on copper foils was purchased from Grolltex Inc.

2. CaF₂ Substrate Preparation

CaF₂ substrates (25 mm diameter with a thickness of 2 mm, PI-KEM Ltd.) were cleaned with acetone, ethanol, and deionized water sequentially in the ultrasonic environment for five minutes. Subsequently, the CaF₂ substrates were immersed in an HCl solution at pH 2 for 2 hours to generate the fresh CaF₂ surface. After that, two 100 nm-thick gold strips were thermally evaporated onto the CaF₂ windows with a shadow mask. The gold strips serve as the reference sample to generate a stable and precise reference phase.

3. Sample Cell

Our sample cell is schematically depicted in Fig. 1a and Fig. S1. The cell mainly consists of two rectangular polytetrafluoroethylene (PTFE) parts, the top clamp part, and the bottom flowing channel (12×3×3 mm³) part. The top clamp has an opening of $\sim 16 \text{ mm}$ in diameter for the light beam paths. The bottom part has two round holes on the left- and right-side walls, serving as the inlet and outlet of nitrogen (N₂), respectively. The prepared sample on a CaF₂ substrate and an O-ring was then sandwiched between the top and the bottom PTFE parts. The O-ring creates a seal between the N₂ or aqueous solution and the air. The base and clamp parts were cleaned with piranha solution before use.

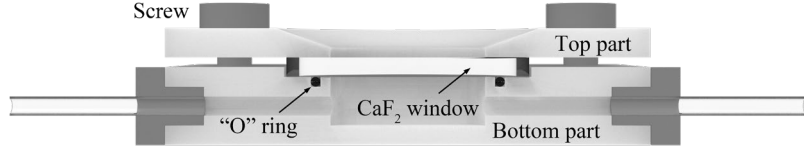


Fig. S1 | Experimental setup. Schematic diagram of the sample cell for Raman and HD-SFG measurements. The inlet of the sample cell is connected to a pipe for purging with N₂ at a flow rate of ~50 μ l/s to remove water vapor in the air.

4. Raman Measurement

The Raman spectra were recorded with a WITec confocal Raman spectrometer (alpha 300 R, $\times 10$ objective) with 600 grooves/mm grating, 532 nm laser, 2 mW power, and 10 s integration time.

5. AFM Measurement

The surface morphology of the graphene samples was measured using an atomic force microscope (AFM, Bruker, JPK) working in the noncontact mode. We used a silicon cantilever (OLYMPUS OMCL-AC 160, $f = 327$ kHz, $k = 27$ N m⁻¹) for the measurement, and the measurement was conducted in the air with a Relative Humidity (RH) of ~25 %.

6. $\chi^{(2)}$ Spectrum Normalization

The total intensity of the signal light measured in the HD-SFG is represented by the sum of sample sum frequency (SF) light and local oscillator (LO) reflected at an interface, which can be expressed as follows:

$$|E_{\text{total}}|^2 = |E_{\text{sample}}|^2 + |r_{\text{sample}}E_{\text{LO}}|^2 + E_{\text{sample}}r_{\text{sample}}^*E_{\text{LO}}^*e^{i\omega T} + E_{\text{sample}}^*r_{\text{sample}}E_{\text{LO}}e^{-i\omega T}, \quad (\text{S1})$$

where E_{sample} and E_{LO} are the electric fields of the SF light from the sample and the LO, respectively. r_{sample} is the reflectivity coefficient of the measured sample for the LO. T is the time delay between SF lights from the sample SF and the LO. The third term on the right-hand side of Eq. S1 was picked up using time-domain filtration with Fourier transform and was then converted to an interferogram through inverse Fourier transform. The measured complex-valued spectra of second-order nonlinear susceptibility ($\chi^{(2)}$) of the CaF₂/water/graphene interfaces were obtained via the Fourier analysis of the obtained interferogram and normalization with that of the CaF₂/gold interface (Eq. S2).

$$\chi^{(2)} = \frac{E_{\text{sample}}r_{\text{sample}}^*E_{\text{LO}}^*e^{i\omega T}}{E_{\text{gold}}r_{\text{gold}}^*E_{\text{LO}}^*e^{i\omega T}}, \quad (\text{S2})$$

where E_{gold} is the electric fields of the SF light from the gold, r_{gold} is the reflectivity coefficient of the gold sample for the LO. The interferogram of the CaF_2 /gold interface was collected at the gold strip region of the sample immediately before the sample measurement to ensure a precise and stable reference phase. The phase of the gold thin film is determined by measuring the O-H stretching $\text{Im}\chi^{(2)}$ spectrum of the CaF_2 -supported graphene/ D_2O interface via normalization of the signal with that of CaF_2 /gold. As D_2O does not have any vibrational response in this region, and its $\chi^{(2)}$ response arises solely from the interface,³⁸ we can determine the phase of gold based on the fact that the $\text{Im}\chi^{(2)}$ spectrum of the CaF_2 -supported graphene/ D_2O interface shows a flat zero line.³² The $\chi^{(2)}$ spectra at the air/suspended graphene/water interface and the air/ D_2O interface were obtained via normalization of the signal with that of air/z-cut quartz.

7. $\chi^{(2)}$ Spectrum Simulation

We carried out SFG spectra simulations for the CaF_2 /water interface, the graphene/water interface, and the nanoconfined water system using *ab initio* molecular dynamics (AIMD) simulations. The AIMD simulations were carried out using the mixed Gaussian and plane wave approach as implemented in the CP2K code.^{39,40} We used the revPBE^{41,42} exchange-correlation (XC) functionals together with the empirical van der Waals (vdW) correction scheme of Grimme's D3(0)⁴³ method. The core electrons were described using the Norm-conserving Goedecker-Teter-Hutter pseudopotentials.^{44,45} We employed the short-ranged MOLOPT double-valance ζ basis with one set of polarization functions (DZVP) and the plane wave density cutoff of 400 Ry. A time step for integrating the equation of motion was set to 0.5 fs. All simulations were performed at 300 K in the NVT ensemble with the thermostat of the canonical sampling through the velocity rescaling method.⁴⁶

We ran AIMD simulations for the three nanoconfined systems with varying water layer thickness, and the CaF_2 /aqueous LiCl solution and graphene/aqueous LiCl solution interfaces. For all the systems, we used the same simulation cell, where the cell vectors were $\vec{a} = (14.76 \text{ \AA}, 0 \text{ \AA}, 0 \text{ \AA})$, $\vec{b} = (7.38 \text{ \AA}, 12.78 \text{ \AA}, 0 \text{ \AA})$, and $\vec{c} = (0 \text{ \AA}, 0 \text{ \AA}, 50 \text{ \AA})$. \vec{a} and \vec{b} formed the surface, while \vec{c} formed the surface normal. This surface unit cell (\vec{a} and \vec{b}) corresponds to the graphene-*p*(6×6) hexagonal cell. The lattice mismatch between the graphene sheet and the $\text{CaF}_2(111)$ surface was compensated by compressing the $\text{CaF}_2(111)$ -*p*(4×4) by 4.5%. We used the $\text{CaF}_2(111)$ surface, as it is the most thermodynamically stable surface.⁴⁷ The CaF_2 part consists of three layers (one layer is composed of 16

formula units of CaF_2), while the graphene sheet is composed of 72 carbon atoms. Since the $\text{CaF}_2(111)$ surface is positively charged, we detached one fluorine atom from the CaF_2 surface and made the fluorine ions solvated in water.

For the small-size nanoconfined water sample, we contained 49 H_2O molecules and 2 pairs of Li^+ and Cl^- ions. For the intermediate size nanoconfined water sample, we contained 77 H_2O molecules and 3 pairs of Li^+ and Cl^- ions. For the large-size nanoconfined water sample, we contained 99 H_2O molecules and 4 pairs of Li^+ and Cl^- ions. For the graphene-water sample, we contained 136 H_2O molecules. For the CaF_2 -water sample, we contained 159 H_2O molecules and 3 pairs of Li^+ and Cl^- ions. The resulting thickness of the vacuum regions is >15 Å (see Supplementary Discussion S3). As a result, the other side of the interfaces for the CaF_2 /water and graphene/water samples which are generated in the slab geometry is the water/air interface. We generated 5 independent configurations for each sample. We equilibrated the systems by running 5 ps and we sampled the >30 ps trajectories, from which we computed the SFG spectra and did the analysis.

For computing the SFG spectra, we used the surface-specific velocity-velocity correlation function approach, which enables us to compute the SFG spectra in a short length of the trajectories.⁴⁸ The SFG response where $\chi_{xxz}^{(2),R}(\omega)$ can be written as:

$$\chi_{xxz}^{(2),R}(\omega) = \frac{Q(\omega)\mu'(\omega)\alpha'(\omega)}{i\omega^2} \chi_{xxz}^{SSVVCF}(\omega) \quad (\text{S3})$$

$$\chi_{xxz}^{SSVVCF}(\omega) = \int_0^{\infty} dt e^{-i\omega t} \left\langle \sum_{i,j} g_{ds}(z_i(0)) \dot{r}_{z,i}^{OD}(0) \frac{\vec{r}_j^{OD}(t) \cdot \vec{r}_j^{OD}(t)}{|\vec{r}_j^{OD}(t)|} \right\rangle \quad (\text{S4})$$

$g_{ds}(z_i)$ is the truncation function for the dividing surface to selectively extract the vibrational responses of water molecules near the interface:

$$g_{ds}(z_i) = \begin{cases} 0 & \text{for } z_i \geq z_{ds} \\ 1 & \text{for } z_i < z_{ds} \end{cases} \quad (\text{S5})$$

where z_{ds} is the z-coordinate of the dividing surface and z_i is the z-coordinate of the i th O atom. The z_{ds} value was set to decouple the responses of CaF_2 /water interface and graphene/water interface from the water/air interface. Note that for the confined water system, we did not use any dividing surface, the SFG response is calculated by using the whole water slab. We set the origin point as the averaged position of the first layer of F atoms for the CaF_2 /water interface, and the averaged position of C atoms for the

graphene/water interface. The z_{ds} value is set to 12 Å for both the CaF₂/water system and graphene/water system. Due to the geometry, the $g_{ds}(z_i)$ function for CaF₂/water system is slightly modified as:

$$g_{ds}(z_i) = \begin{cases} 0 & \text{for } z_i \leq -z_{ds} \\ 1 & \text{for } z_i > -z_{ds} \end{cases} \quad (S6)$$

Supplementary Discussion

S1. LiCl Concentration in the Confinement.

The $\text{Im}\chi^{(2)}$ spectrum at the CaF_2/bulk aqueous LiCl solution interface varies with the LiCl concentration when it is below 2 M (Fig. S2). For a fair comparison of the CaF_2/bulk water signal and the confined water signal, we need to estimate the LiCl concentration in confinement. We can calculate an upper limit to the concentration based on the volume ($\sim 0.2 \mu\text{L}$, 10 mM) of LiCl solution trapped between the graphene sheet and the CaF_2 substrate during sample preparation, as well as the final size ($\sim 0.8 \text{ nm} \times 20 \text{ mm} \times 15 \text{ mm}$) of the nanoconfinement. The volume was calculated from the density of 10 mM LiCl solution and the measured mass difference of the freshly prepared sample before and after drying. Using this approach, the LiCl solution is estimated to be approximately 8.3 M. The actual LiCl concentration is likely lower due to some LiCl precipitation at the edges and folds in the graphene sample (Fig. S3). Double-check from the Raman spectrum (Fig. S2b) of the nanoconfined LiCl solution at the thicker water layer region with a height of few hundreds of nanometers (Fig. S3f) indicates the $\sim 5 \text{ M}$ concentration. We stress that for a channel of few hundreds of nanometers height, confinement effect on water is negligible,⁸ and the comparison of the Raman spectrum with that of bulk solution is very plausible. Assuming that the ion concentration at different regions in the gap between the CaF_2 substrate and the graphene sheet is similar, we used a 5 M LiCl solution to measure the $\text{Im}\chi^{(2)}$ spectrum at the CaF_2/bulk aqueous LiCl solution interface and the bulk aqueous LiCl solution/graphene interface for comparison with the confined water signal. We stress within the range of conceivable salt (2-8 M) concentrations, our conclusion (eq. (1)) holds (see Extended Data Fig. 3).

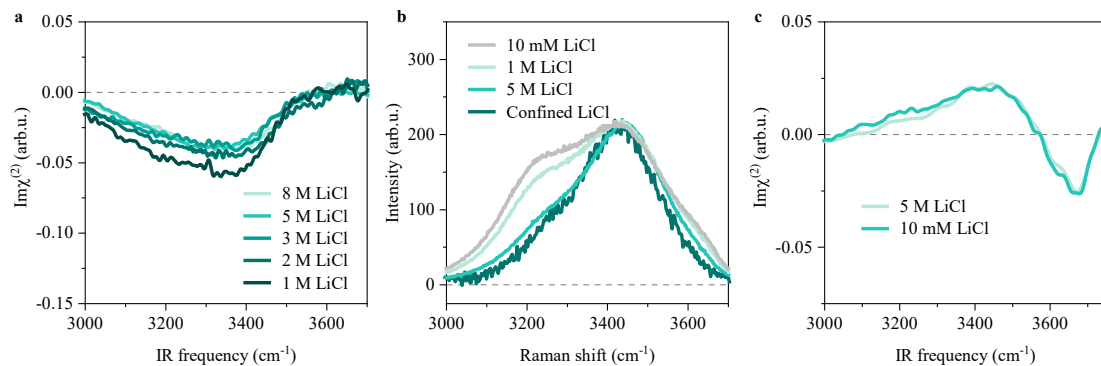


Fig. S2 | LiCl Concentration in the Confinement. **a.** The $\text{Im}\chi^{(2)}$ spectrum at the CaF_2/bulk aqueous LiCl solution interface at different ion concentrations. The dashed line serves as the zero line. **b.** Raman spectra of bulk LiCl aqueous solutions at different concentrations compared to the Raman spectrum of

the nanoconfined LiCl solution at the thicker water layer region. All the Raman spectra were normalized according to the peak intensity ($\sim 3450 \text{ cm}^{-1}$) for comparison. **c.** The $\text{Im}\chi^{(2)}$ spectrum at the bulk aqueous LiCl solution/graphene interface at different ion concentrations. The dashed line serves as the zero line.

S2. AFM Characterization of the Graphene Sample.

To obtain the thickness of the confined water sandwiched by the monolayer graphene sheet and the CaF_2 substrate, we measured the surface topology of the graphene deposited on the CaF_2 substrate using AFM. An optical image of the graphene sample is shown in Fig. S3a and the AFM image at the indicated regions in the optical image is presented in Fig. S3b-f. The AFM image indicates the bare CaF_2 surface is atomic flat with some atomic terraces (indicated by green arrows) and the surface roughness is 0.2 nm (Fig. S3b and Fig. S3g). At the edges of the graphene, dotlike thicker features (black arrows) and folds (red arrows) appear. At the graphene sheet region, although dotlike thicker features (black arrows) and wrinkles (white arrows) are occasionally present, graphene spread atomically flat on the CaF_2 substrate over large areas with a surface roughness of 0.30 nm (Fig. S3d). The optical image shows that the large area can be up to several millimeters (Fig. S3a). The wrinkles with a typical height of a few nanometers are commonly observed in CVD graphene.^{49,50} The dotlike thicker features are likely the precipitated ions as such features are hardly seen in graphene samples without being exposed to LiCl solution during the wetting transfer.

Although the graphene spread atomically flat on the CaF_2 substrate over large areas, some cracks (purple arrows) and thicker water layer ((blue arrows) with a height of tens of nanometers and a size of a few hundred nanometers may appear (Fig. S3e-g). In the SFG experiments, a spot of $\sim 100 \mu\text{m}$ diameter was probed, and care was taken via the double check with AFM to ensure that the SFG probed region contained predominantly the $\sim 1 \text{ nm}$ confined water without the appearance of the cracks and the thicker nanobubbles (Fig. S3d). We emphasize that the AFM image near the cracks shows that the height difference between the regions where a graphene sheet covers and does not is around 1.2 nm (Fig. S3g). This result is consistent with the AFM image at the edges of the graphene sample (Fig. 1b) that the graphene and CaF_2 create an $8 \pm 3 \text{ \AA}$ confinement.

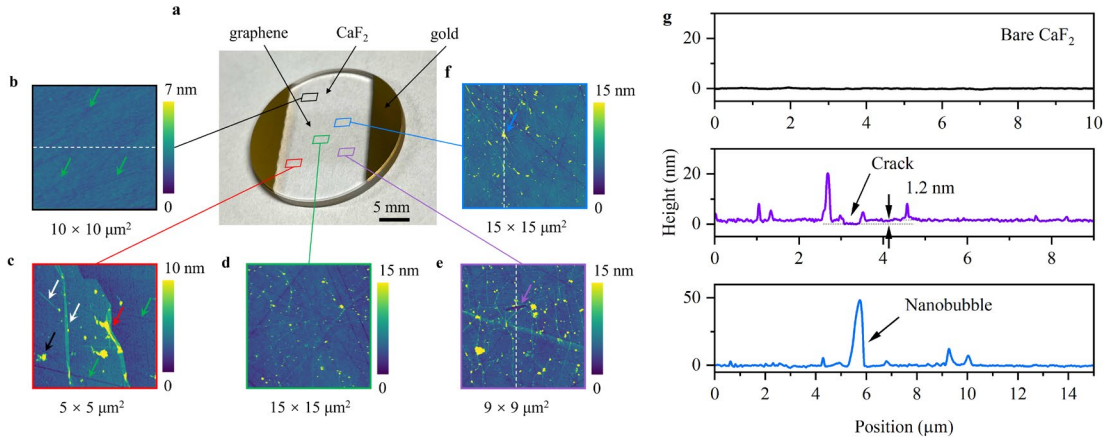


Fig. S3 | AFM Characterization of the Graphene Sample. **a.** Optical image of the graphene sample. **b-e.** AFM image of **(b)** the bare CaF₂ substrate and **(c-f)** the indicated region of the graphene monolayer deposited on the CaF₂ substrate. **(g).** The height profiles along the white dashed line in **b, e** and **f**. Measurements were conducted at ambient conditions.

S3. Additional Simulation Data

Figure S4 plots the profiles of the number density along the surface normal axis. The origin points of the axis were set to the center of mass for the water molecules in the cell.

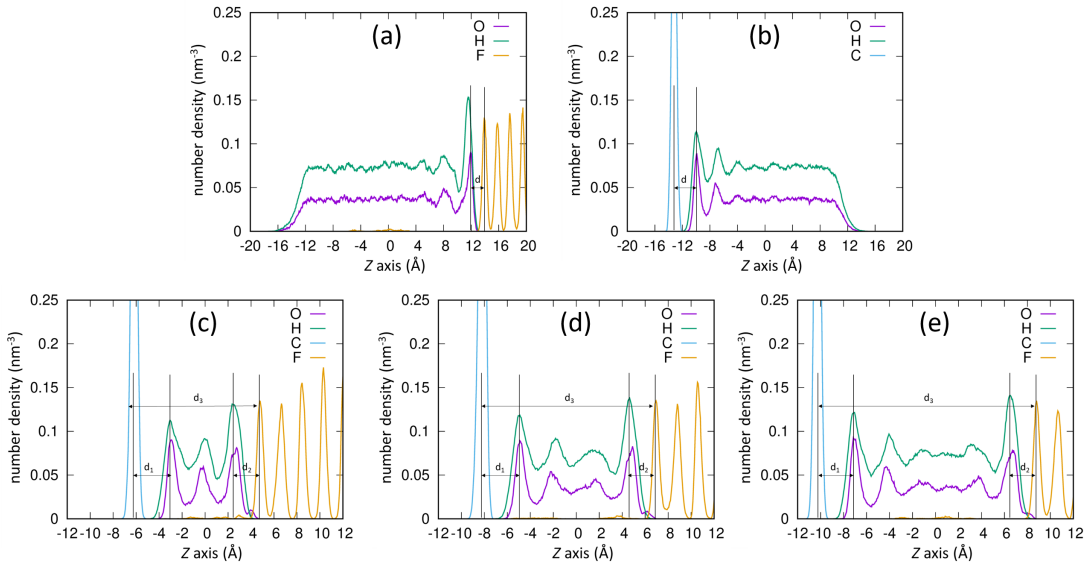


Fig. S4 | The axial profiles of the number density for (a) the CaF₂/water interface system, (b) the water/graphene interface as well as (c-e) the nanoconfined systems containing (c) 49, (d) 77, and (e) 99 water molecules. Note that the number density of the Ca atom is not shown here to make the figure

clearer. The distances between water slab and graphene are (b) $d=3.29\text{\AA}$, (c) $d_1=3.21\text{\AA}$, (d) $d_1=3.25\text{\AA}$, (e) $d_1=3.24\text{\AA}$. The distances between water slab and CaF_2 are (a) $d=1.97\text{\AA}$, (c) $d_2=2.16\text{\AA}$, (d) $d_2=2.20\text{\AA}$, (e) $d_2=2.16\text{\AA}$. The distances between the graphene and CaF_2 in the confined water systems are (c) $d_3=10.93\text{\AA}$, (d) $d_3=15.08\text{\AA}$, (e) $d_3=19.07\text{\AA}$.

S4. Raman Characterization of the Graphene Sample.

Confinement of water molecules between the graphene monolayer and the CaF_2 substrate is supposed to induce changes in the strain (ε) and charge density (n) of the graphene monolayer. The changes in ε and n will cause the frequency shift of the Raman G-band (ω_G , $\sim 1582\text{ cm}^{-1}$) and 2D-band (ω_{2D} , $\sim 2678\text{ cm}^{-1}$). Accordingly, to probe the effect of confined water on the graphene sheet, we measured Raman G-band and 2D-band. The data collected at a randomly selected region is shown in Fig. S5. A blue-shift of ω_G and ω_{2D} is observed compared to the graphene supported on a CaF_2 substrate without water molecules being confined.

As increasing n (ε) of an intrinsic graphene, its values of (ω_G, ω_{2D}) will move from O along v_H (v_S) as shown in Fig. S5, where v_H (v_S) represents the unit vector for n (ε) in the ω_G - ω_{2D} vector space. ε and n on the graphene can be independently determined^{50,51} through correlation analysis of the frequency shift of ω_G and ω_{2D} . The variations in ω_G and ω_{2D} of the CVD graphene on the CaF_2 substrate are purely induced by strain with negligible charge doping ($n < 10^{12}\text{ cm}^{-2}$). Most graphene experiences a compressive strain varying from 0 to 0.05% due to the presence of dense wrinkles in CVD graphene. Situation becomes different when water molecules were confined between the graphene monolayer and the CaF_2 substrate. In this case, at most regions, graphene experiences a tensile strain ranging from 0 to 0.05% owing to the successful confinement of water molecules. Such a tensile strain enables us to approximately determine the vdW pressure experienced by the trapped solution to be 0 to 500 MPa.⁵² Besides the variation along the v_S , most data points move towards v_h , indicating a slight hole doping ($n^{\text{hole}} \sim 2 \times 10^{12}\text{ cm}^{-2}$). The Raman spectral analysis of the graphene monolayer again verify the successful confinement of water molecules between the graphene monolayer and the CaF_2 substrate.

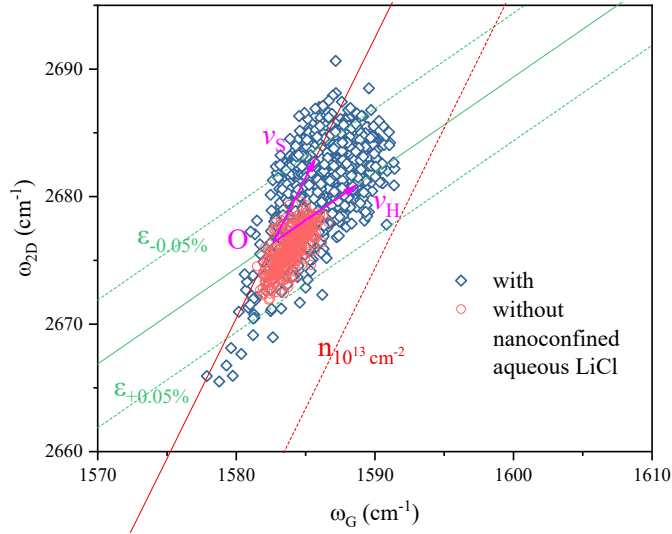


Fig. S5 | Raman characterization of the graphene sample. Correlation analysis of the frequency shift of ω_G and ω_{2D} . The red and green lines represent the correlation induced by pure strain and hole doping effects respectively. Point *O* represents the intrinsic frequencies of the G- and 2D-bands that are not affected by strain or charges and are $1,581.8\text{ cm}^{-1}$ and $2,676.9\text{ cm}^{-1}$, respectively.⁵³ The averaged strain-sensitivity factor G-band is $-69.1 \pm 3.4\text{ cm}^{-1}/\%$.⁵⁴ The positive charge-sensitivity factor of the G-band is adopted from a reference (red dashed line).⁵³

S5. Amplitude Calibration of the SFG Spectra at ssp Polarization

The sample HD-SFG spectra at *ssp* polarization were normalized with that for the gold at *ssp* polarization according to Eq. S2. To obtain the absolute value of the effective surface non-linear susceptibilities, one needs to calibrate the amplitude of the normalized spectra ($\chi^{(2)}$) via;

$$\chi_{ssp, \text{eff}}^{(2)} = \chi^{(2)} \frac{r_{\text{CaF}_2/\text{gold}} \chi_{ssp, \text{eff}, \text{CaF}_2/\text{gold}}^{(2)}}{r_{\text{sample}}}, \quad (S7)$$

where $\chi_{ssp, \text{eff}, \text{CaF}_2/\text{gold}}^{(2)}$ is the effective SFG signal at the CaF_2/gold interface, r is the reflectivity coefficient for the s-polarized LO beam and can be obtained via;

$$r = \frac{n_i \cos \theta_i - n_j \cos \theta_i}{n_i \cos \theta_i + n_j \cos \theta_j}, \quad (S8)$$

To get $\chi_{ssp,eff}^{(2)}$, one needs to know the $r_{\text{CaF}_2/\text{gold}}\chi_{ssp,eff,\text{CaF}_2/\text{gold}}^{(2)}$ which is an unknown value. Here, we obtain the $r_{\text{CaF}_2/\text{gold}}\chi_{ssp,eff,\text{CaF}_2/\text{gold}}^{(2)}$ in the following three steps:

1. To obtain the absolute value of the effective surface non-linear susceptibilities at the air/D₂O interface ($\chi_{ssp, \text{eff, air/D}_2\text{O}}^{(2)}$), we calibrate the amplitude of the normalized spectra ($\chi_{D_2\text{O}, zqz}^{(2)}$) via;

$$\chi_{ssp,eff,air/D_2O}^{(2)} = i\chi_{D_2O,zqz}^{(2)} \frac{r_{air/zqz} |\chi_{ssp,eff,air/zqz}^{(2)}|}{r_{air/D_2O}}, \quad (S9)$$

where r_{air/D_2O} and $r_{air/zqz}$ are the reflectivity of LO at the air/D₂O interface and the air/z-cut quartz interface, respectively. $\chi_{D_2O,zqz}^{(2)}$ is the measured spectrum at the air/D₂O interface normalized by the signal at the air/z-cut quartz interface. $\chi_{ssp,eff,air/zqz}^{(2)}$ is the effective SFG signal at the air/z-cut quartz interface which is a known value and can be calculated from the parameters listed in Tables S1 and Eq. S10;

$$\chi_{ssp,eff,air/zqz}^{(2)} = 2L_{yy}(\omega_{SF})L_{yy}(\omega_{vis})L_{xx}(\omega_{IR}) \cos \theta_i(\omega_{IR}) \chi_q^{(2)} l_c, \quad (S10)$$

where $\chi_q^{(2)} \approx 8 \times 10^{-13} \text{ mV}^{-1}$ is the second-order susceptibility of the z-cut quartz. ω_{SF} , ω_{vis} , and ω_{IR} are the frequency of the corresponding beam, respectively. θ_i is the incident angle of the IR beam in bulk medium i . L_{ii} ($i = x, y, z$) is the ii component of the Fresnel coefficients, and is given by;

$$L_{xx} = \frac{2n_i \cos \theta_j}{n_i \cos \theta_j + n_j \cos \theta_i}, \quad (S11)$$

$$L_{yy} = \frac{2n_i \cos \theta_i}{n_i \cos \theta_i + n_j \cos \theta_j}, \quad (S12)$$

$$L_{zz} = \frac{2n_j \cos \theta_i}{n_j \cos \theta_i + n_i \cos \theta_j} \frac{n_i^2}{n'^2}, \quad (S13)$$

where θ_j is the refracted angle of corresponding light (SF, vis, IR) in bulk medium j . n_i and n_j are the refractive index of corresponding light in bulk medium i and bulk medium j . n' is the refractive index of the interfacial layer. The beam configuration of the SFG measurement is displayed in Fig. S6.

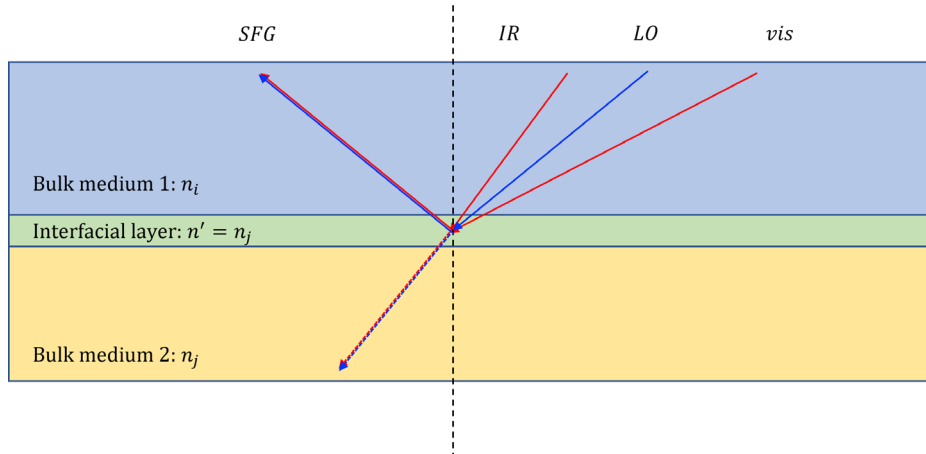


Fig. S6 | The beam configuration of the non-collinear HD-SFG measurement.

The effective coherence length for the reflected SFG, l_c is calculated by;

$$l_c = \frac{1}{k_{2z}(\omega_{SF}) + k_{2z}(\omega_{vis}) + k_{2z}(\omega_{IR})} \approx 43 \text{ nm.} \quad (\text{S14})$$

k_{2z} is the wavevector of corresponding lights in medium j along the z -axis. By using Eqs. S10-S14 and the parameters listed in Table S1-2, we obtain $\chi_{ssp,eff,air/zqz}^{(2)} = 5.6 \times 10^{-21} \text{ m}^2\text{V}^{-1}$. From Eq. S9, we obtain $\chi_{ssp,eff,air/D_2O}^{(2)} = 7.2 \times 10^{-23} \text{ m}^2\text{V}^{-1}$.

2. Assuming that $\chi_{yyz}^{(2)}$ is the same at the $\text{CaF}_2/\text{D}_2\text{O}$ interface and at the air/ D_2O interface, one can get

$$\chi_{yyz,D_2O}^{(2)} = \frac{\chi_{ssp,eff,CaF_2/D_2O}^{(2)}}{F_{CaF_2/D_2O}} = \frac{\chi_{ssp,eff,air/D_2O}^{(2)}}{F_{air/D_2O}}, \quad (\text{S15})$$

where $\chi_{ssp,eff,CaF_2/D_2O}^{(2)}$ is the effective non-resonant SFG signal from the $\text{CaF}_2/\text{D}_2\text{O}$ interface. F is the Fresnel factor and is given by;

$$F = L_{yy}(\omega_{SF})L_{yy}(\omega_{vis})L_{zz}(\omega_{IR}) \sin \theta_i(\omega_{IR}), \quad (\text{S16})$$

Using Eqs. S15-S16, we obtain $\chi_{ssp,eff,CaF_2/D_2O}^{(2)} = 2.7 \times 10^{-22} \text{ m}^2\text{V}^{-1}$.

3. To obtain the absolute value of the effective surface non-linear susceptibilities at the CaF_2/gold interface ($\chi_{ssp,eff,CaF_2/gold}^{(2)}$), we calibrate the amplitude of the normalized spectra ($\chi_{D_2O,gold}^{(2)}$) via;

$$\chi_{ssp,eff,CaF_2/gold}^{(2)} = \frac{r_{CaF_2/D_2O}\chi_{ssp,eff,CaF_2/D_2O}^{(2)}}{r_{CaF_2/gold}\chi_{D_2O,gold}^{(2)}}, \quad (\text{S17})$$

where $r_{\text{CaF}_2/\text{D}_2\text{O}}$ is the reflectivity of LO at the $\text{CaF}_2/\text{D}_2\text{O}$ interface. $\chi_{D_2O,gold}^{(2)}$ is the measured spectrum at the $\text{CaF}_2/\text{D}_2\text{O}$ interface normalized by the signal at the CaF_2/gold interface.

From these three steps, we finally obtain;

$$r_{CaF_2/gold}\chi_{ssp,eff,CaF_2/gold}^{(2)} = 3.2 \times 10^{-20} \text{ m}^2\text{V}^{-1}. \quad (\text{S18})$$

Table S1 Incident angles used to calculate the Fresnel factors

Incident angle θ	Vis (800 nm)	IR (3300 nm)
air	64°	50°
CaF_2	38.9°	32.8°

Table S2 Refractive indexes used to calculate the Fresnel factors for the CaF_2 /water, CaF_2 /air, air/water and air/z-cut quartz interfaces

Refractive index n	SF (~635 nm)	Vis (800 nm)	IR (3300 nm)
CaF_2	1.43	1.43	1.42
H_2O	1.33	1.33	1.40
D_2O	1.33	1.33	1.25
z-cut quartz	1.54	1.54	1.52
air	1	1	1

S6. Extraction of $\chi_{yyz}^{(2)}$ Component.

The effective SFG signal ($\chi_{ssp,\text{eff}}^{(2)}$) at the *ssp* polarization is given by;

$$\chi_{ssp,\text{eff}}^{(2)} = F \chi_{yyz}^{(2)}, \quad (\text{S19})$$

Note that the interfacial dielectric constant ($\varepsilon' = n'^2$) is critical to do the Fresnel factor corrections and to extract the amplitude of the yyz components of the measured $\chi^{(2)}$ spectra ($\chi_{yyz}^{(2)}$). Two homogeneous interfacial dielectric constant models, the Lorentz model ($n' = n_j$) and the Slab model ($n' = \sqrt{\frac{n_i^2(n_i^2+5)}{4n_i^2+2}}$), are usually employed.^{34,35} Such corrections and underlying assumptions of the interfacial dielectric constant^{36,37} critically affect the SFG amplitude. For the *ssp* polarization combination, our recent studies show that the Lorentz model allows for more accurate Fresnel factor corrections at aqueous interfaces,³⁶ while the slab model underestimates the H-bonded O–H stretch signal. Therefore, in this work, the Lorentz model is employed to do the Fresnel factor corrections at all different sample geometries.

For the air/suspended graphene/water interface, we consider it as the air/water interface to do the Fresnel factor corrections because the monolayer graphene with one-atom thickness hardly affects the corrections.⁵⁵ The interface layer at the CaF_2 /confined-water/graphene interfaces are intricate, comprising two interfaces: CaF_2 /confined-water and confined-water/graphene, which raises the question of whether one homogeneous interfacial dielectric constant can accurately capture the interface layer. To address this question, we measured the conventional SFG signals ($|\chi_{ssp,\text{eff},\text{CaF}_2/\text{water}/\text{graphene}}^{(2)}|^2$) at the CaF_2 /confined-water/graphene interface and compared it with the signal ($|\chi_{ssp,\text{eff},\text{graphene}/\text{water}/\text{CaF}_2}^{(2)}|^2$) obtained from the same sample but with graphene positioned on top (Fig. S7).

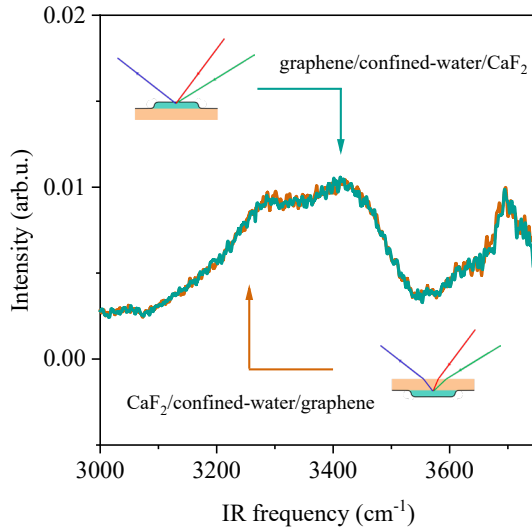


Fig. S7 | Conventional SFG signals at the $\text{CaF}_2/\text{confined-water}/\text{graphene}$ interface and the $\text{graphene}/\text{confined-water}/\text{CaF}_2$ interface. The insets show the corresponding sample geometries.

In both sample geometries, the spectral lineshape remains consistent. After eliminating the Fresnel factor by considering a CaF_2/air interface and air/CaF_2 interface, respectively (Eq. S11-S13, S16, and S19), the spectral amplitudes are also consistent (Fig. S7). These results indicate that one homogeneous interfacial dielectric constant is sufficient to capture the sub-nanometer thickness interface layer, and the Lorentz model is accurate for the Fresnel factor corrections for the $\text{CaF}_2/\text{confined-water}/\text{graphene}$ interfaces.

S7. Tuning the Thickness of Nanoconfined Water.

The thickness of the nanoconfined water was tuned by progressively lowering the RH in the sample cell (Fig. 1d and Fig. S1) by increasing the N_2 flowing rate. The higher the flow rate, the lower the RH in the sample cell and the thinner the thickness of the nanoconfined water. To this end, we measured the thickness of nanoconfined water at different N_2 flowing rates using AFM. To be consistent with the HD-SFG measurement, the AFM measurements were conducted after purging the N_2 at different flowing rates for more than 2 hours and were measured immediately within 10 minutes after the sample was demounted from the sample cell. To avoid the water thickness change, the RH was maintained to be lower than 25 % during the AFM measurements. The measured thickness of the nanoconfined water on the same sample as a function of the N_2 flowing rate is shown in Fig. S8a and the AFM data is shown in Fig. S8b. The thickness of the nanoconfined water decreases from $\sim 8 \text{ \AA}$ to below 3 \AA when increases the flowing rate from 0.1 mL/s to 5 mL/s .

For comparison with the nanoconfined water signal, we measured the $\text{Im}\chi_{yyz}^{(2)}$ spectra at the CaF_2 /water vapor interface. For this measurement, the freshly cleaned CaF_2 substrate was mounted on the sample cell. For a fair comparison with the nanoconfined water signal, the $\text{Im}\chi_{yyz}^{(2)}$ spectrum at the CaF_2 /water vapor interface was measured at the same N_2 flowing rate. The data is shown in Fig. S8c. At 0.1 mL/s, the $\text{Im}\chi_{yyz}^{(2)}$ spectrum exhibits a broad negative H-bonded O-H band ranging from 3000 to 3550 cm^{-1} , similar to the signal at the CaF_2 /bulk water interface. Furthermore, a high-frequency negative peak at around 3700 cm^{-1} appears. Its frequency and its sign indicate that the peak arises from the free O-H of outmost water at the water vapor/air interface.⁵⁶ We note that the spectral features differ from the $\sim 8 \text{ \AA}$ confined water signal implying that the probed $\text{Im}\chi_{yyz, \text{confined}}^{(2)}$ spectrum arises from nanoconfined water. Raising the flowing rate to 2 mL/s, the H-bonded O-H band decreases and the free O-H disappears due to the further evaporation of water on the CaF_2 surface. Still, the H-bonded O-H band is stronger than that of the below 3 \AA confined water signal. The weakened H-bonded O-H band for the below 3 \AA confined water signal is consistent with the hypothesis that the $<8 \text{ \AA}$ confinement forces the confined water to lie flat with O-H groups parallel to the graphene and the CaF_2 substrate, yielding zero SFG signals.

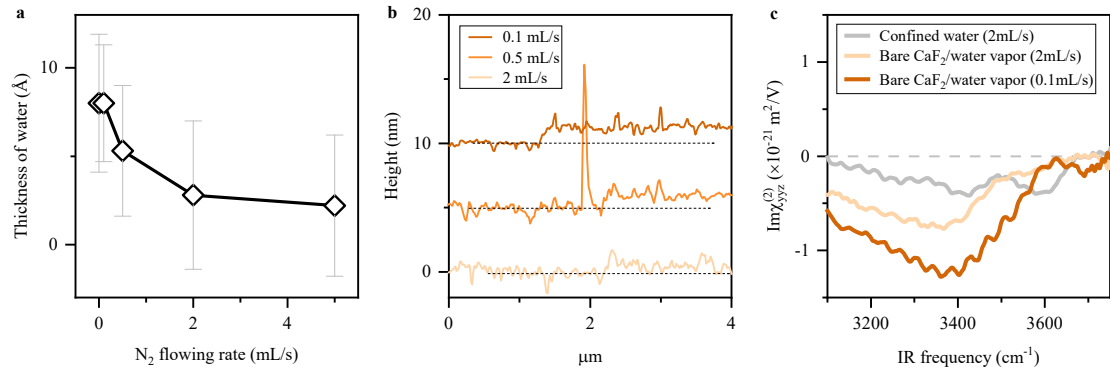


Fig. S8 | Tuning the thickness of the nanoconfined water. **a.** Thickness of the nanoconfined water as a function of the N_2 flowing rate. The thicknesses of the nanoconfined water were measured on the same sample and were calculated assuming the graphene thickness of $\sim 0.34 \text{ nm}$. **b.** Corresponding AFM height profiles probing the graphene edges. **c.** $\text{Im}\chi_{yyz}^{(2)}$ spectra measured at the CaF_2 /water vapor interface under different N_2 flowing rates. The dashed lines in **b** and **c** serve as the zero lines.

References

1. Verdaguer, A., Sacha, G. M., Bluhm, H. & Salmeron, M. Molecular Structure of Water at Interfaces: Wetting at the Nanometer Scale. *Chem. Rev.* **106**, 1478–1510 (2006).
2. Xu, K., Cao, P. & Heath, J. R. Graphene visualizes the first water adlayers on mica at ambient conditions. *Science* **329**, 1188–1191 (2010).
3. Giovambattista, N., Rossky, P. J. & Debenedetti, P. G. Effect of pressure on the phase behavior and structure of water confined between nanoscale hydrophobic and hydrophilic plates. *Phys. Rev. E* **73**, 041604 (2006).
4. Kapil, V. *et al.* The first-principles phase diagram of monolayer nanoconfined water. *Nature* **609**, 512–516 (2022).
5. Takaiwa, D., Hatano, I., Koga, K. & Tanaka, H. Phase diagram of water in carbon nanotubes. *Proc. Natl. Acad. Sci.* **105**, 39–43 (2008).
6. Algara-Siller, G. *et al.* Square ice in graphene nanocapillaries. *Nature* **519**, 443 (2015).
7. Chmiola, J. Anomalous Increase in Carbon Capacitance at Pore Sizes Less Than 1 Nanometer. *Science* **313**, 1760–1763 (2006).
8. Fumagalli, L. *et al.* Anomalously low dielectric constant of confined water. *Science* **360**, 1339–1342 (2018).
9. Robin, P., Kavokine, N. & Bocquet, L. Modeling of emergent memory and voltage spiking in ionic transport through angstrom-scale slits. *Science* **373**, 687–691 (2021).
10. Lim, C. H. Y. X., Nesladek, M. & Loh, K. P. Observing High-Pressure Chemistry in Graphene Bubbles. *Angew. Chem. Int. Ed.* **53**, 215–219 (2014).
11. Beaumont, M. *et al.* Unique reactivity of nanoporous cellulosic materials mediated by surface-confined water. *Nat. Commun.* **12**, 2513 (2021).
12. Kobayashi, J. *et al.* A Microfluidic Device for Conducting Gas-Liquid-Solid Hydrogenation Reactions. *Science* **304**, 1305–1308 (2004).
13. Dalla Bernardina, S. *et al.* Water in Carbon Nanotubes: The Peculiar Hydrogen Bond Network Revealed by Infrared Spectroscopy. *J. Am. Chem. Soc.* **138**, 10437–10443 (2016).
14. Mallamace, F. *et al.* Evidence of the existence of the low-density liquid phase in supercooled, confined water. *Proc. Natl. Acad. Sci.* **104**, 424–428 (2007).
15. Han, S., Choi, M. Y., Kumar, P. & Stanley, H. E. Phase transitions in confined water nanofilms. *Nat. Phys.* **6**, 685–689 (2010).
16. Robin, P. *et al.* Long-term memory and synapse-like dynamics in two-dimensional nanofluidic channels. *Science* **379**, 161–167 (2023).
17. Duan, C. & Majumdar, A. Anomalous ion transport in 2-nm hydrophilic nanochannels. *Nat. Nanotechnol.* **5**, 848–852 (2010).

18. Muñoz-Santiburcio, D. & Marx, D. Confinement-Controlled Aqueous Chemistry within Nanometric Slit Pores. *Chem. Rev.* **121**, 6293–6320 (2021).
19. Chialvo, A. A. & Vlcek, L. Can We Describe Graphene Confined Water Structures as Overlapping of Approaching Graphene–Water Interfacial Structures? *J. Phys. Chem. C* **120**, 7553–7561 (2016).
20. Ohto, T., Tada, H. & Nagata, Y. Structure and dynamics of water at water–graphene and water–hexagonal boron-nitride sheet interfaces revealed by ab initio sum-frequency generation spectroscopy. *Phys. Chem. Chem. Phys.* **20**, 12979–12985 (2018).
21. Wang, Y. *et al.* Chemistry governs water organization at a graphene electrode. *Nature* **615**, E1–E2 (2023).
22. Shen, Y. R. Surface properties probed by second-harmonic and sum-frequency generation. *Nature* **337**, 519–525 (1989).
23. Yamaguchi, S. & Tahara, T. Heterodyne-detected electronic sum frequency generation: “Up” versus “down” alignment of interfacial molecules. *J. Chem. Phys.* **129**, 101102 (2008).
24. Du, Q., Superfine, R., Freysz, E. & Shen, Y. R. Vibrational spectroscopy of water at the vapor/water interface. *Phys. Rev. Lett.* **70**, 2313 (1993).
25. Du, Q., Freysz, E. & Shen, Y. R. Surface Vibrational Spectroscopic Studies of Hydrogen Bonding and Hydrophobicity. *Science* **264**, 826–828 (1994).
26. Das, B., Ruiz-Barragan, S. & Marx, D. Deciphering the Properties of Nanoconfined Aqueous Solutions by Vibrational Sum Frequency Generation Spectroscopy. *J. Phys. Chem. Lett.* **14**, 1208–1213 (2023).
27. Bonn, M., Nagata, Y. & Backus, E. H. G. Molecular Structure and Dynamics of Water at the Water–Air Interface Studied with Surface-Specific Vibrational Spectroscopy. *Angew. Chem. Int. Ed.* **54**, 5560–5576 (2015).
28. Aluru, N. R. *et al.* Fluids and Electrolytes under Confinement in Single-Digit Nanopores. *Chem. Rev.* **123**, 2737–2831 (2023).
29. Liang, X. *et al.* Toward Clean and Crackless Transfer of Graphene. *ACS Nano* **5**, 9144–9153 (2011).
30. Zhang, Y., de Aguiar, H. B., Hynes, J. T. & Laage, D. Water Structure, Dynamics, and Sum-Frequency Generation Spectra at Electrified Graphene Interfaces. *J. Phys. Chem. Lett.* **11**, 624–631 (2020).
31. Nihonyanagi, S. (二本柳聰史), Yamaguchi, S. (山口祥一) & Tahara, T. (田原太平). Direct evidence for orientational flip-flop of water molecules at charged interfaces: A heterodyne-detected vibrational sum frequency generation study. *J. Chem. Phys.* **130**, 204704 (2009).
32. Wang, Y. *et al.* Direct Probe of Electrochemical Pseudocapacitive pH Jump at a Graphene Electrode**. *Angew. Chem. Int. Ed.* **62**, e202216604 (2023).
33. Ohno, K., Okimura, M., Akai, N. & Katsumoto, Y. The effect of cooperative hydrogen bonding on the OH stretching-band shift for water clusters studied by matrix-isolation infrared spectroscopy and density functional theory. *Phys. Chem. Chem. Phys.* **7**, 3005–3014 (2005).

34. Yu, C.-C. *et al.* Polarization-Dependent Heterodyne-Detected Sum-Frequency Generation Spectroscopy as a Tool to Explore Surface Molecular Orientation and Ångström-Scale Depth Profiling. *J. Phys. Chem. B* **126**, 6113–6124 (2022).

35. Chiang, K.-Y. *et al.* The dielectric function profile across the water interface through surface-specific vibrational spectroscopy and simulations. *Proc. Natl. Acad. Sci.* **119**, e2204156119 (2022).

36. Yu, X., Chiang, K.-Y., Yu, C.-C., Bonn, M. & Nagata, Y. On the Fresnel factor correction of sum-frequency generation spectra of interfacial water. *J. Chem. Phys.* **158**, 044701 (2023).

37. Zhuang, X., Miranda, P. B., Kim, D. & Shen, Y. R. Mapping molecular orientation and conformation at interfaces by surface nonlinear optics. *Phys. Rev. B* **59**, 12632–12640 (1999).

38. Adhikari, A. Accurate determination of complex $\chi^{(2)}$ spectrum of the air/water interface. *J. Chem. Phys.* **143**, 124707 (2015).

39. Kühne, T. D. *et al.* CP2K: An electronic structure and molecular dynamics software package - Quickstep: Efficient and accurate electronic structure calculations. *J. Chem. Phys.* **152**, 194103 (2020).

40. Hutter, J., Iannuzzi, M., Schiffmann, F. & VandeVondele, J. cp2k: atomistic simulations of condensed matter systems. *Wiley Interdiscip. Rev. Comput. Mol. Sci.* **4**, 15–25 (2014).

41. Perdew, J. P., Burke, K. & Ernzerhof, M. Generalized Gradient Approximation Made Simple. *Phys. Rev. Lett.* **77**, 3865–3868 (1996).

42. Zhang, Y. & Yang, W. Comment on “Generalized gradient approximation made simple”. *Phys. Rev. Lett.* **80**, 890 (1998).

43. Grimme, S., Antony, J., Ehrlich, S. & Krieg, H. A consistent and accurate ab initio parametrization of density functional dispersion correction (DFT-D) for the 94 elements H-Pu. *J. Chem. Phys.* **132**, 154104 (2010).

44. Goedecker, S., Teter, M. & Hutter, J. Separable dual-space Gaussian pseudopotentials. *Phys. Rev. B* **54**, 1703 (1996).

45. Krack, M. Pseudopotentials for H to Kr optimized for gradient-corrected exchange-correlation functionals. *Theor. Chem. Acc.* **114**, 145–152 (2005).

46. Bussi, G., Donadio, D. & Parrinello, M. Canonical sampling through velocity rescaling. *J. Chem. Phys.* **126**, 014101 (2007).

47. Khatib, R. *et al.* Water orientation and hydrogen-bond structure at the fluorite/water interface. *Sci. Rep.* **6**, 24287 (2016).

48. Ohto, T., Usui, K., Hasegawa, T., Bonn, M. & Nagata, Y. Toward ab initio molecular dynamics modeling for sum-frequency generation spectra; an efficient algorithm based on surface-specific velocity-velocity correlation function. *J. Chem. Phys.* **143**, 124702 (2015).

49. Ahn, G. *et al.* Optical Probing of the Electronic Interaction between Graphene and Hexagonal Boron Nitride. *ACS Nano* **7**, 1533–1541 (2013).

50. Calado, V. E., Schneider, G. F., Theulings, A. M. M. G., Dekker, C. & Vandersypen, L. M. K. Formation and control of wrinkles in graphene by the wedging transfer method. *Appl. Phys. Lett.* **101**, 103116 (2012).
51. Wang, C., Liu, Y., Lan, L. & Tan, H. Graphene wrinkling: formation, evolution and collapse. *Nanoscale* **5**, 4454–4461 (2013).
52. Vasu, K. S. *et al.* Van der Waals pressure and its effect on trapped interlayer molecules. *Nat. Commun.* **7**, 12168 (2016).
53. Lee, J. E., Ahn, G., Shim, J., Lee, Y. S. & Ryu, S. Optical separation of mechanical strain from charge doping in graphene. *Nat. Commun.* **3**, 1024 (2012).
54. Zabel, J. *et al.* Raman spectroscopy of graphene and bilayer under biaxial strain: bubbles and balloons. *Nano Lett.* **12**, 617–621 (2012).
55. Moloney, E. G., Azam, Md. S., Cai, C. & Hore, D. K. Vibrational sum frequency spectroscopy of thin film interfaces. *Biointerphases* **17**, 051202 (2022).
56. Ji, N., Ostroverkhov, V., Tian, C. S. & Shen, Y. R. Characterization of Vibrational Resonances of Water-Vapor Interfaces by Phase-Sensitive Sum-Frequency Spectroscopy. *Phys. Rev. Lett.* **100**, 096102 (2008).